

Classification of Atomic Density Distributions Using Scale Invariant Blob Localization

Kai Cordes¹, Oliver Topic², Manuel Scherer²
Carsten Klempt², Bodo Rosenhahn¹, and Jörn Ostermann¹

¹ Institut für Informationsverarbeitung (TNT), Leibniz Universität Hannover
<http://www.tnt.uni-hannover.de>

² Institut für Quantenoptik (IQO), Leibniz Universität Hannover
<http://www.iqo.uni-hannover.de>

Abstract. We present a method to classify atomic density distributions using CCD images obtained in a quantum optics experiment. The classification is based on the scale invariant detection and precise localization of the central blob in the input image structure. The key idea is the usage of an a priori known shape of the feature in the image scale space. This approach results in higher localization accuracy and more robustness against noise compared to the most accurate state of the art blob region detectors.

The classification is done with a success rate of 90% for the experimentally captured images. The results presented here are restricted to special image structures occurring in the atom optics experiment, but the presented methodology can lead to improved results for a wide class of pattern recognition and blob localization problems.

1 Introduction

1.1 Atomic Density Distributions

Satyendranath Bose and Albert Einstein predicted in 1924 that a gas of atoms with integer spin forms a so-called Bose-Einstein condensate (BEC) when it is cooled to ultra cold temperature [1]. Below a certain temperature threshold, a large fraction of atoms confined in an external trap occupy the physical ground state. In 1995, two experimental groups achieved Bose-Einstein condensation of trapped dilute atomic gases [2,3] after cooling it below a temperature of $1 \mu\text{K}$. At these temperatures, the velocity distribution is very narrow and due to Heisenberg's uncertainty relation [4] the spatial distributions of those atoms is broad. Typically, it extends to several tens of micrometers, making it possible to image the ensemble with a CCD camera as shown in Fig. 1.

In the past years, BEC's consisting of atoms with non-zero spin attracted a lot of notice. These atoms behave like little magnets that may be oriented perpendicular to an external magnetic field. Atomic collisions can now generate pairs of atoms, with one spin pointing upwards and the other one downwards. This process was identified to be a parametric amplifier for classical seed atoms

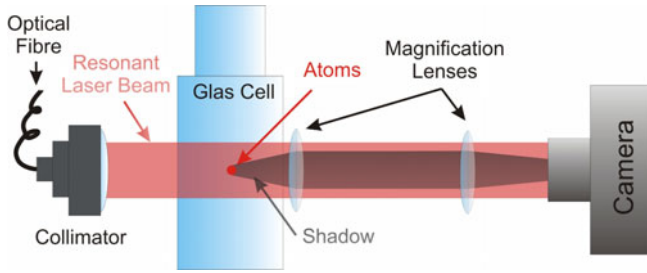


Fig. 1. Simplified sketch of the imaging system. The atomic cloud is illuminated by collimated resonant laser light from an optical fibre. The shadow from the atoms is imaged by a magnifying lens system onto a CCD-Camera. Subtraction from an image without atoms leads to the atomic density distribution.

or vacuum fluctuations [5,6]. Depending on the magnetic field, those atoms can be generated in different states with different characteristic probability distributions [7]. In the cylindrical trapping geometry used in the recent experiments, the discrete physical states that may be populated have density distributions $n(r)$ which can be approximated with the following expression

$$n_{nl}(\mathbf{r}) \propto J_l^2(\beta_{nl} \frac{|\mathbf{r}|}{r_{\text{tf}}}) \quad (|\mathbf{r}| < r_{\text{tf}}), \quad (1)$$

where J_l are the Bessel functions of the first kind and β_{nl} is the n th zero of J_l . The size is scaled by the radius r_{tf} . Each distribution is identified by two quantum numbers n and l for the radial excitation and the rotation of the cloud.

After preparing the clouds, the trap is switched off to allow for ballistic expansion, where the distribution is stretched but not perturbed [8]. During the expansion, the three spin components are separated by an applied magnetic field gradient and then irradiated with a resonant laser beam. The atomic clouds absorb light and the resulting shadow is imaged onto a CCD camera. From the CCD data, the density distribution can be determined. The imaging technique has three deficiencies: Interferences in the detection beam produce regular stripes on the density distribution. The imaging setup can distort the image slightly. The finite number of detected photons leads to shot noise on the images.

In general, we detect pictures with clouds in arbitrary combinations of quantum numbers. Fig. 2 shows the three examples under investigation (I_0 , I_1 , and I_2) with the quantum numbers $(n, l) = (1, 0)$, $(2, 0)$, and $(2, 1)$. For the interpretation of the experimental results, an unambiguous classification of the quantum numbers is of key interest. This classification should be independent of the total position and the size of the clouds, since these parameters are quickly changed by a variation of the experimental parameters and technical uncertainties. Additionally, the classification should be robust with respect to the experimental noise on the figures. In the following, we describe how the density distribution can be classified automatically and the quantum numbers are inferred.

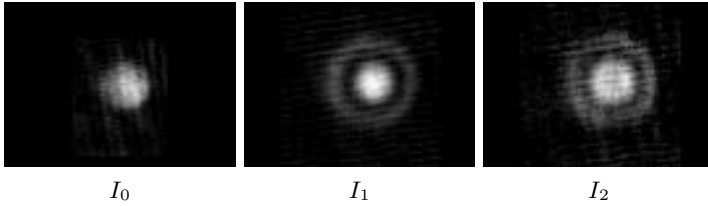


Fig. 2. Real atomic distribution shapes to be detected and classified. From left to right: type I_0 , I_1 , and I_2 . *Best viewed on a LCD.*

1.2 Feature and Blob Detectors

The objective of this work is to classify the three different atomic distribution shape types I_0 , I_1 , and I_2 as shown in Fig. 2. For each distribution shape, the underlying function is known from equation (1). The shapes I_0 and I_1 are identical (proportional to $J_0^2(\cdot)$), but differ by the radial excitation. The shape of I_2 is proportional to $J_1^2(\cdot)$. As the size of the blobs can vary, it is necessary to perform a scale invariant classification. Due to the currently small available data set, a training scheme for the classification is not applied and the proposed approach concentrates on feature estimation. The **contributions** are:

- a new detector robust to noise for the localization of one unique feature of known shape with high accuracy,
- the comparison of the detector to the most accurate state of the art blob detectors using synthetic images, and
- the classification of atomic distribution shapes using the extracted shape parameters in a unified feature detection framework.

The initial and most important task is the accurate localization of the central blob in the images. Then, the classification can be done in two steps. First, the type of extremum in the input image is determined to separate the types I_0 , I_1 from I_2 . Second, the ring surrounding the blob is localized and used for the separation of type I_0 (no ring visible) and I_1 (ring is visible).

Due to noise and the imaging setup, the target structure might be slightly slanted. Thus, the desired method for the detection task has to be an affine invariant noise resistant blob region detector. In literature, extensive work has been done on region detectors and their evaluation. An overview of most of these detectors can be found in [9], in which the most accurate affine invariant blob detectors are found to be the Hessian-Affine [10] and the MSER [11]. Their evaluations show excellent performance [9,12] regarding the *Repeatability* rate, which is the most often used criterion for elliptical region localization accuracy. In [11], maximally stable extremal regions (MSER) are constructed using a segmentation process. Then, an ellipse is fit to each of the detected regions. Based on affine normalization, the Hessian-Affine detector determines the elliptical shape with the second moment matrix of the intensity gradient. The features are detected as extrema in the scale space, which is introduced and described by Lindeberg et al. [13,14]. The scale space representation is built by cascading

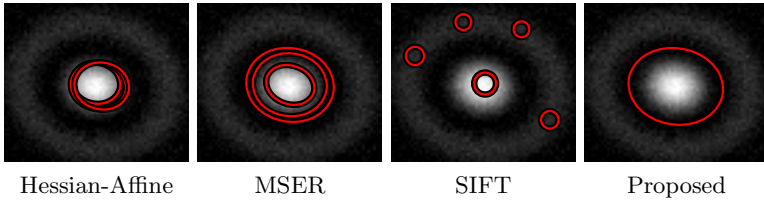


Fig. 3. Localization results of state of the art blob detectors. From left to right: Hessian-Affine, MSER, SIFT, and the proposed approach which aims to localize the first zeros of the input feature. *Best viewed on a LCD.*

Gaussian filters of differing standard deviation σ . The scale space is also used by the SIFT detector [15] as the basis for blob detection. In SIFT, the Difference of Gaussians (*DoG*) pyramid is evaluated as an approximation of the scale space of the input image. A scale space extremum is detected as a luminance value that is bigger or smaller than its 26 neighbors in the *DoG* pyramid. Although the SIFT detector is not affine invariant by design, it shows impressive performance for features with moderate affine distortion. In [16], the localization accuracy of SIFT is increased using a bivariate approximation of the image gradient signal. This approach is adapted for the localization of the feature shapes occurring in the atom optics experiment.

Results of the state of the art blob detectors for an example are shown in Fig. 3. While the Hessian-Affine, MSER, and SIFT detectors lead to ambiguous results, the desired method provides an unique and accurate detection of the central blob, which is defined by the bounding zeros.

Our work demonstrates, that the elliptical shape of these features can be determined with high accuracy by incorporating the knowledge of the underlying functions. It is shown that all three input feature types (Fig. 2) approximately depict the same shape in the dominant scale in the scale space, which leads to a unified detection and localization procedure. Incorporating shape knowledge of the input data, the ring area surrounding the center blob can be determined and used for the classification. In the following Section 2, the approach of localization and classification of the distribution shapes is presented. Section 3 shows experimental results using synthetically constructed and real image data. In Section 4, the paper is concluded.

2 Localization and Classification of Atomic Density Distribution Shapes

A blob feature as shown in Fig. 3 is defined by image coordinates (x_0, y_0) , and the covariance matrix $\Sigma = \begin{pmatrix} a^2 & b \\ b & c^2 \end{pmatrix}$, which determines the elliptical shape. In order to estimate these parameters of the input feature, it has to be detected and localized in the scale space. Here, the Difference of Gaussians (*DoG*) representation is

used, which is a good approximation as proved by the SIFT approach [15]. An experimental analysis using the SIFT scale selection technique (Section 2.1) leads to the proposed function model which approximates the image signal in the selected scale of the DoG . The function model used for the localization is explained in Section 2.2. A robust technique for the detection and localization is derived in Section 2.3. On basis of the extracted localization parameters, the classification of the atomic distributions is done as explained in Section 2.4.

2.1 Feature Shape in the Scale Space

The feature selection scheme of the SIFT detector provides the best representation of a feature in the scale space. The scale is determined by the octave o and the interval i [15]. In Fig. 4, the selected scales for the synthetic input features \tilde{I}_0 , \tilde{I}_1 , and \tilde{I}_2 (top row) are shown in the bottom row. The returned shapes of the input features \tilde{I}_0 , \tilde{I}_1 , \tilde{I}_2 are approximately sinc functions. This observation leads to the assumption for the approximation of a feature in the scale space as shown in the following Section 2.2. Note, that the central blob in the input images lead to minimas in the scale space for all feature types $\tilde{I}_0, \tilde{I}_1, \tilde{I}_2$.

2.2 Localization Using the SINC Function Model

Following the observation that the returned shapes in the Difference of Gaussians pyramid are approximately sinc functions (Section 2.1), the input features

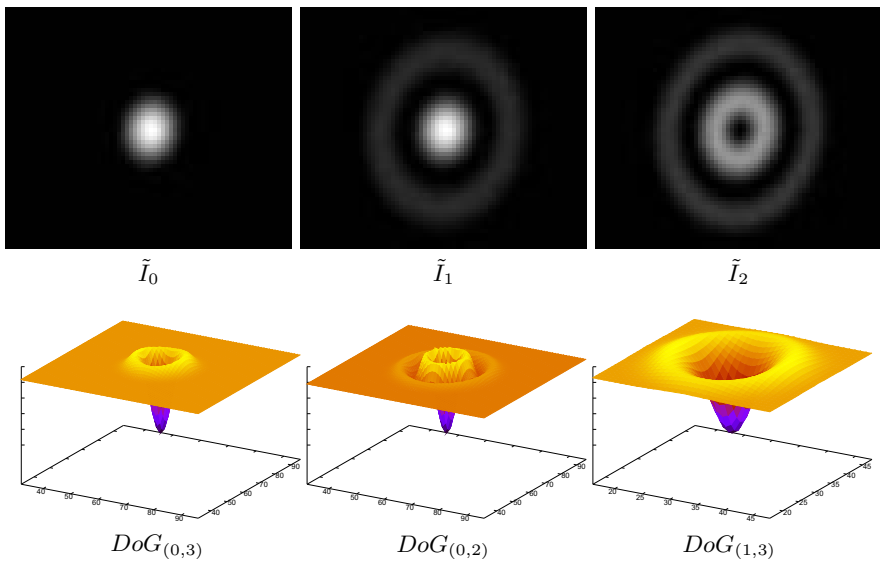


Fig. 4. Resulting image signal $DoG_{(o,i)}$ of interval i in octave o using the scale selection of SIFT. The synthetic test images are shown on top. Each of the input features $\tilde{I}_0, \tilde{I}_1, \tilde{I}_2$ depict a sinc $(r) = \frac{\sin r}{r}$ shape in the selected scale (bottom).

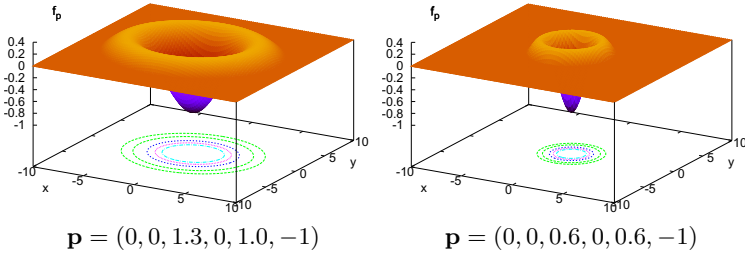


Fig. 5. Proposed regression function $f_{\mathbf{p}}(\mathbf{x})$ for the approximation of the scale space shapes of the input blobs as shown in Fig. 4. Two examples with different covariance matrix Σ are shown.

are localized using this function model. To allow elliptical feature shapes, the covariance matrix $\Sigma = \begin{pmatrix} a^2 & b \\ b & c^2 \end{pmatrix}$ is incorporated. For the following, the abbreviation $R_{\mathbf{x}_0, \Sigma}(\mathbf{x}) := (\mathbf{x} - \mathbf{x}_0)^\top \Sigma^{-1}(\mathbf{x} - \mathbf{x}_0)$ is used. $R_{\mathbf{x}_0, \Sigma}(\mathbf{x})$ is used to describe the elliptical shape with the center coordinate $\mathbf{x}_0 = (x_0, y_0)$. Together with a peak value v , the parameter vector $\mathbf{p} = (x_0, y_0, a, b, c, v)$ determines a member of the following proposed function model $f_{\mathbf{p}}$ for the detection and localization approach:

$$f_{\mathbf{p}}(\mathbf{x}) = \begin{cases} v \cdot \frac{\sin \sqrt{R_{\mathbf{x}_0, \Sigma}(\mathbf{x})}}{\sqrt{R_{\mathbf{x}_0, \Sigma}(\mathbf{x})}}, & \text{for } R_{\mathbf{x}_0, \Sigma}(\mathbf{x}) \leq t_0 \\ 0 & , \text{ otherwise} \end{cases} \quad (2)$$

with $t_0 = 2\pi$. Note, that the peak value v has to be negative $v < 0$ to detect the desired extremum (see Fig. 4). Scale space maxima are not considered for the localization. Two examples for the function model $f_{\mathbf{p}}$ are shown in Fig. 5. They are determined by the parameter vector $\mathbf{p} = (x_0, y_0, a, b, c, v)$ with six components. The parameter vector \mathbf{p} of an input feature is identified by means of a regression analysis. Each fullpel position in each octave o and each interval i is assumed as a possible initialization for the Levenberg-Marquardt optimization algorithm. The covariance matrix is initialized with the unit matrix $\Sigma = \mathbf{E}$, which is equivalent to circular shape. As each scale is normalized in the DoG pyramid, the initial value for v is -1 . The Levenberg-Marquardt (LM) algorithm minimizes the distance $e_{\mathbf{p}}$ between the model function $f_{\mathbf{p}}(\mathbf{x})$ and the image signal $DoG_{(o,i)}(\mathbf{x})$ in the current scale (o, i) evaluating a squared neighborhood \mathcal{N} :

$$e_{\mathbf{p}} = \sum_{\mathbf{x} \in \mathcal{N}} (f_{\mathbf{p}}(\mathbf{x}) - DoG_{(o,i)}(\mathbf{x}))^2 \quad (3)$$

The LM algorithm stops returning the optimal parameter vector \mathbf{p}_{opt} and a residuum value $e_{\mathbf{p}_{opt}}$ which provides a quality measure of the obtained regression function $f_{\mathbf{p}_{opt}}(\mathbf{x})$ for the initial starting position.

In contrast to the SIFT detector, our approach using a regression analysis is capable of evaluating arbitrary neighborhood sizes. As can be seen in Fig. 4, a

neighborhood \mathcal{N} of at least 9×9 pixels is needed to capture the characteristics of the blob shape in the image pyramid. A large neighborhood also leads to a localization which is less sensitive to noise. The SIFT detector uses a 3×3 neighborhood and the neighboring scales to determine the subpel and subscale localization. To compensate for the computational expense of a larger neighborhood, our approach omits to estimate a subscale parameter.

2.3 Feature and Scale Selection

The regression analysis described in Section 2.2 returns a residuum $e_{\mathbf{p}_{opt}}$ for the optimal parameter vector \mathbf{p}_{opt} , which is a quality measure for the resulting regression function $f_{\mathbf{p}_{opt}}(\mathbf{x})$. Hence, the best blob location is found by minimizing the residuum for all possible positions. For the detection of the central blob, it is crucial to favor a scale space minimum in smaller scales. Therefore, the function to be minimized is weighted by the scale $w_{scl} = 2^{o+\frac{1}{k}}$, where k is the number of scales per octave [15] (usually $k = 3$):

$$w_{scl} \cdot e_{\mathbf{p}_{opt}} \rightarrow MIN \quad (4)$$

To ensure optimal solutions, a brute force search is performed within a search range. The brute force search and the large neighborhood lead to a significant increase in computational complexity. This is not critical for the presented classification application.

2.4 Classification of the Feature Shapes

The classification workflow is shown in Fig. 6. Two evaluations are done after localizing the best feature blob. First, the feature type I_2 is distinguished from the others by determining the **Curvature** of the input image at the localized position. This is done by evaluating the first scale of the *DoG* pyramid at the ground plane position $\mathbf{x}_G = \mathbf{x}_0 \cdot 2^o$. To reduce the influence of noise, the median \mathcal{N}_{med} in a 3×3 neighborhood \mathcal{N} is used to classify between $I_0 \cup I_1$ (concave curvature) and I_2 (convex curvature):

$$\mathcal{N}_{med}(DoG_{(0,0)}(\mathbf{x}_G)) \leq 0 \Rightarrow I_0 \cup I_1 \quad (5)$$

$$\mathcal{N}_{med}(DoG_{(0,0)}(\mathbf{x}_G)) > 0 \Rightarrow I_2 \quad (6)$$

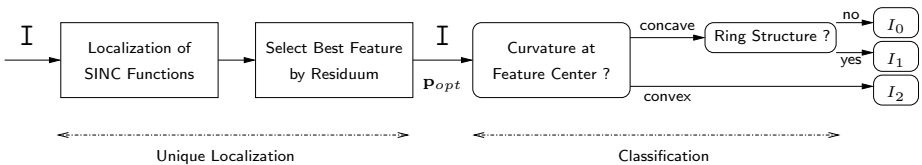


Fig. 6. Workflow diagram of localization and classification of the input image I

The classification between I_0 and I_1 is done by evaluating if there is a **Ring Structure** around the center blob or not. The Ring \mathcal{S} is localized as the region between the first zeros z_{01} and the second zeros z_{02} of the Bessel function $J_0(\cdot)$:

$$\mathcal{S} = \{\mathbf{x} : z_{01} \leq \sqrt{\frac{R_{\mathbf{x}_G, q \cdot \Sigma_G(\mathbf{x})}}{D(q \cdot \Sigma_G)}} \leq z_{02}\} \quad (7)$$

where $\Sigma_G = \Sigma \cdot 2^\circ$ is the covariance matrix of the feature in the image ground plane and $D(\cdot)$ denotes the determinant. The zeros of $J_0(\cdot)$ are known as $z_{01} \approx 2.40$ and $z_{02} \approx 5.52$. The ellipse scaling factor $q \approx 1.59$ maps the minima of the Bessel function $J_0(\cdot)$ to its first zeros and is calculated as the quotient of the first minimum and the first zero z_{01} of $J_0(\cdot)$. The region \mathcal{S} is localized after the central blob is accurately determined by \mathbf{p}_{opt} .

An example of the elliptical ring \mathcal{S} using relation (7) is shown in Fig. 9. Using this area, the two feature types I_0 and I_1 can be distinguished by analyzing the gray values inside \mathcal{S} . Therefore, the energy $E_{\mathcal{S}}$ of the image signal $\mathbf{I}(\mathbf{x})$ inside the Ring \mathcal{S} is calculated and a threshold classifier with threshold thr is applied. The area $A_{\mathcal{S}}$ of the Ring \mathcal{S} is used for the normalization of $E_{\mathcal{S}}$ to obtain scale invariant energy values:

$$E_{\mathcal{S}} = \frac{1}{A_{\mathcal{S}}} \int_{\mathcal{S}} |\mathbf{I}(\mathbf{x})|^2 d\mathbf{x} \quad (8)$$

If $E_{\mathcal{S}} < thr$, then the feature is of type I_0 , otherwise it is of type I_1 . The threshold thr can be chosen between 10 and 25 which is valid for all the experimental feature data in this paper as shown in Fig. 8.

3 Experimental Results

For the evaluation of our method, synthetic and real data is used. For the synthetic data, the ground truth localization of each feature is known. The detection accuracy of position $\mathbf{x}_G = (x_G, y_G)$ and shape Σ_G is shown using the *Surface Error* measure [10]. The *Surface Error* is a percentage value that is minimal if a detected ellipse area is exactly matching the ellipse determined by the ground truth values. The evaluation for the three different types of synthetic input features $\tilde{I}_0, \tilde{I}_1, \tilde{I}_2$ with added Gaussian noise is shown in Section 3.1. The spatial neighborhood \mathcal{N} evaluated for the feature localization is set to 13×13 pixels. For the real data, classification results of a set of images captured in the atom optics experiment are shown in Section 3.2. The processing time for an image (size 128×128) on common PC hardware is about 10 seconds, which is not critical for an automatic evaluation.

3.1 Results of Synthetic Data

Synthetic test images of types \tilde{I}_0, \tilde{I}_1 , and \tilde{I}_2 as shown in Fig. 4 (top row) are constructed using equation (1) and a cutoff at the first zeros for \tilde{I}_0 and second zeros for \tilde{I}_1, \tilde{I}_2 , respectively. For the evaluation, the following variations of the image signal are generated:

- scale s : $2 \leq s \leq 9$ (3 octaves) with step size 0.5
- subpel position x_0 : $-0.5 \leq x_0 < 0.5$ with step size 0.04
- noise variance σ_n : $0 \text{ dB} \leq \sigma_n \leq 80 \text{ dB}$ with step size 20 dB

Each of the variations has an impact on the localization accuracy. The subpel variation is to emphasize the signal approximation scheme used by the detectors while the scale variation emphasizes the scale invariance. The noise scenario demonstrates the robustness against image noise. For each synthetically constructed image, the feature is slightly slanted using a covariance Matrix Σ with $\frac{a}{c} = 1.2$.

For the classification task, it is crucial to select one unique feature for further evaluation, which is done by our method by design. The numbers of features selected by the presented approaches are shown in Fig. 7, top row. For the other detectors the numbers depend on the feature type and on the noise level. The localization accuracy evaluation is shown in Fig. 7, bottom row. If multiple features are detected by a method, the best of them is chosen for the evaluation. The cases in which no feature is detected are discarded from this evaluation (small scales for *Hessian-Affine*). To avoid the dependency on a global scale of the features, a normalization is applied to the covariance matrix results.

Our approach provides an accurate and reliable localization for each feature type compared to the best possible result of each of the other detectors. Due to the good subpel localization estimation, the SIFT detector provides comparably accurate results, but strongly increasing numbers of features with increasing noise. Interestingly, the localization accuracy of each detector does not increase significantly with increasing Gaussian noise. The detectors *Hessian-Affine* and

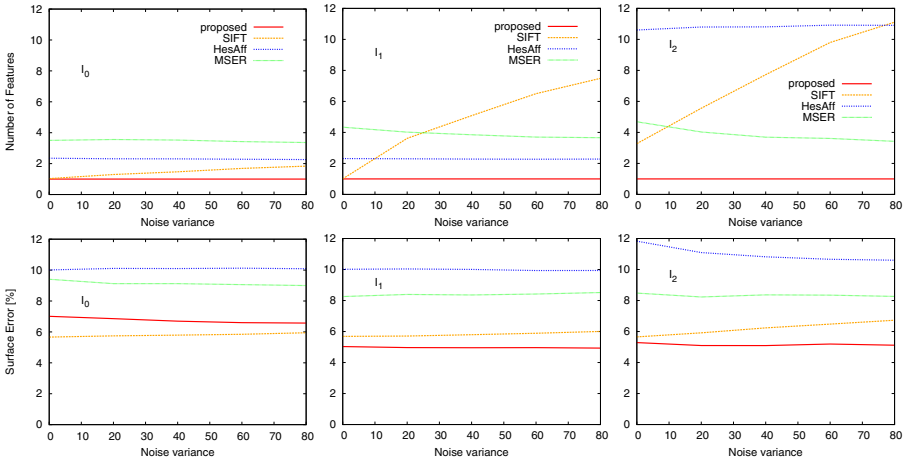


Fig. 7. Comparison of the number of detected features (top row) and the mean *Surface Error* (bottom row) for the three synthetic test features and the four region localization methods. In case of ambiguous detection results, the best is chosen for the *Surface Error*. From left to right: feature types I_0 , I_1 , and I_2

MSER result in highest Surface Errors. We can state that our results provide high accuracy which is robust to synthetic Gaussian image noise.

3.2 Results of Atom Optics Experiment Image Data

The captured image data include the real atom distributions resulting from the quantum optics experiment. To obtain equally distributed scales of features, additional input images are generated by resizing the original data set. To verify the thresholding approach explained in Section 2.4, the energy values E_S in equation (8) are shown in Fig. 8. Obviously, the types I_0 and I_1 are classified reliably and independently from the detected scale.

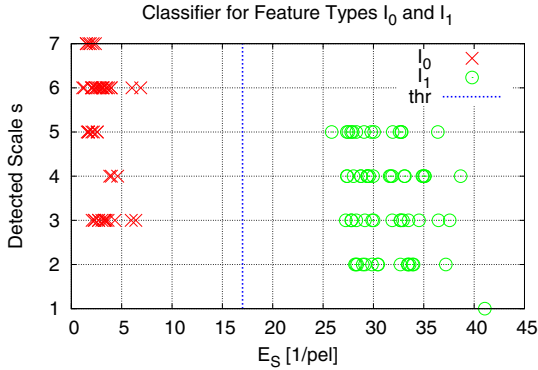


Fig. 8. Energy values E_S for the real experiment data for the feature types I_0 and I_1 of different sizes. It is shown that a simple threshold value thr is sufficient to separate the two classes. The classification is independent of the detected scale.

For the evaluation of the classification, 52 images of each type I_0 , I_1 , and I_2 are available. Examples are shown in Fig. 2. The classification rates for each input feature type and the two classification stages are shown in Table 1. The results for TP_{Curv} and TP_{Ring} demonstrate that misclassifications are only resulting from the curvature estimation in which only a small neighborhood is evaluated. Thus, this evaluation is more sensitive to the strong noise, especially for the input feature type I_2 . The *Ring Structure* detection and evaluation works perfect.

The overall correct classification rate is 90.4%. Classification failures are due to strong noise covering the center shape. In this case, blobs of type I_2 are

Table 1. Classification rate *True Positives* for the two stages *Curvature* TP_{Curv} and *Ring Structure* TP_{Ring} (see Section 2.4) and the resulting classification rate TP_{Σ}

	I_0	I_1	I_2	Σ
TP_{Curv}	96.2%	75.0%	85.6	
TP_{Ring}	100%	100%	–	100%
TP_{Σ}	96.2%	100%	75.0%	90.4%

very similar to the type I_1 (see Fig. 2). Understanding and modeling the noise structure, i.e. regular stripes from laser beam interferences, will improve the classification and is left for future works. Examples of the detected *Ring Structure* \mathcal{S} which is used to classify the features types I_0, I_1 are shown in Fig. 9.

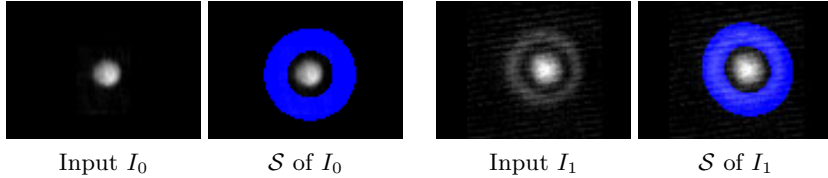


Fig. 9. Examples of the detected *Ring Structure* \mathcal{S} (in blue) around the central blob for two experimentally captured input images. *Best viewed on a LCD.*

4 Conclusion

The presented method consists of the detection, localization, and classification of atomic distribution shapes resulting from three types of modes from a quantum optics experiment. Therefore, a new feature detector is developed based on the SIFT approach. The a priori known shapes of the input features are incorporated using a regression analysis with a derived function model for the gradient signal. The determination of the function model parameters leads to a reliable and accurate localization of the elliptical shape of a feature blob. The shape parameters are used as input data for a simple two stage classifier.

The presented detector shows superior localization accuracy and noise robustness compared to the most accurate state of the art blob detectors. This is demonstrated using synthetic images. The classification success rate is 90% for the real data resulting from the atom optics experiment.

Our approach provides a useful application of scale invariant feature localization in the field of quantum optics. Future works will incorporate the noise structure for further classification improvements.

We acknowledge support from the Centre for Quantum Engineering and Space-Time Research QUEST.

References

1. Einstein, A.: Quantentheorie des einatomigen idealen gases. In: Sitzungsberichte der Preußischen Akademie der Wissenschaften Physikalisch-mathematische Klasse, pp. 261–267 (1924)
2. Anderson, M.H., Ensher, J.R., Matthews, M.R., Wieman, C.E., Cornell, E.A.: Observation of bose-einstein condensation in a dilute atomic vapor. *Science* 269, 198–201 (1995)
3. Davis, K.B., Mewes, M.O., Andrews, M.R., van Druten, N.J., Durfee, D.S., Kurn, D.M., Ketterle, W.: Bose-einstein condensation in a gas of sodium atoms. *Physical Review Letters* 75, 3969–3973 (1995)

4. Heisenberg, W.: Über den anschaulichen inhalt der quantentheoretischen kinematik und mechanik. *Zeitschrift für Physik* 43, 172–198 (1927)
5. Klempt, C., Topic, O., Gebreyesus, G., Scherer, M., Henninger, T., Hyllus, P., Ertmer, W., Santos, L., Arlt, J.J.: Multiresonant spinor dynamics in a bose-einstein condensate. *Physical Review Letters* 103, 195302 (2009)
6. Klempt, C., Topic, O., Gebreyesus, G., Scherer, M., Henninger, T., Hyllus, P., Ertmer, W., Santos, L., Arlt, J.J.: Parametric amplification of vacuum fluctuations in a spinor condensate. *Physical Review Letters* 104, 195303 (2010)
7. Scherer, M., Lücke, B., Gebreyesus, G., Topic, O., Deuretzbacher, F., Ertmer, W., Santos, L., Arlt, J.J., Klempt, C.: Spontaneous breaking of spatial and spin symmetry in spinor condensates. *Physical Review Letters* 105, 135302 (2010)
8. Castin, Y., Dum, R.: Bose-einstein condensates in time dependent traps. *Physical Review Letters* 77, 5315–5319 (1996)
9. Tuytelaars, T., Mikolajczyk, K.: Local invariant feature detectors: a survey. *Foundations and Trends in Computer Graphics and Vision*, vol. 3 (2008)
10. Mikolajczyk, K., Schmid, C.: Scale & affine invariant interest point detectors. *International Journal of Computer Vision (IJCV)* 60, 63–86 (2004)
11. Matas, J., Chum, O., Urban, M., Pajdla, T.: Robust wide baseline stereo from maximally stable extremal regions. In: *British Machine Vision Conference (BMVC)*, vol. 1, pp. 384–393 (2002)
12. Mikolajczyk, K., Tuytelaars, T., Schmid, C., Zisserman, A., Matas, J., Schaffalitzky, F., Kadir, T., Gool, L.V.: A comparison of affine region detectors. *International Journal of Computer Vision (IJCV)* 65, 43–72 (2005)
13. Lindeberg, T.: Feature detection with automatic scale selection. *International Journal of Computer Vision (IJCV)* 30, 79–116 (1998)
14. Lindeberg, T., Garding, J.: Shape-adapted smoothing in estimation of 3-d shape cues from affine deformations of local 2-d brightness structure. *Image and Vision Computing (IVC)* 15, 415–434 (1997)
15. Lowe, D.G.: Distinctive image features from scale-invariant keypoints. *International Journal of Computer Vision (IJCV)* 60, 91–110 (2004)
16. Cordes, K., Müller, O., Rosenhahn, B., Ostermann, J.: Bivariate feature localization for sift assuming a gaussian feature shape. In: *Bebis, G., Boyle, R., Parvin, B., Koracin, D., Chung, R., Hammoud, R., Hussain, M., Kar-Han, T., Crawfis, R., Thalmann, D., Kao, D., Avila, L. (eds.) ISVC 2010. LNCS, vol. 6453, pp. 264–275. Springer, Heidelberg (2010)*